Diffraction phase microscopy: retrieving phase contours on living cells with a wavelet-based space-scale analysis

Cristina Martinez-Torres, Lotfi Berguiga, Laura Streppa, Elise Boyer-Provera, Laurent Schaeffer, Juan Elezgaray, Alain Arneodo, Françoise Argoul

Journal of Biomedical Optics

SPIEDigitalLibrary.org/jbo

Diffraction phase microscopy: retrieving phase contours on living cells with a wavelet-based space-scale analysis

Cristina Martinez-Torres
Lotfi Berguiga
Laura Streppa
Elise Boyer-Provera
Laurent Schaeffer
Juan Elezgaray
Alain Arneodo
Françoise Argoul

Diffraction phase microscopy: retrieving phase contours on living cells with a wavelet-based space-scale analysis

Cristina Martinez-Torres,[a] Lotfi Berguiga,[b] Laura Streppa,[a,c] Elise Boyer-Provera,[a] Laurent Schaeffer,[c] Juan Elezgaray,[d] Alain Arneodo,[a] and Françoise Argoul[a,*]
[a]Université de Lyon, CNRS UMR5672, ENS de Lyon, 69007 France
[b]Université de Lyon, CNRS USR3010, ENS de Lyon, 69007 France
[c]Université de Lyon, CNRS UMR5239, ENS de Lyon, 69007 France
[d]Université Bordeaux 1-ENITAB, CNRS UMR 5248, Pessac, 33600 France

Abstract. We propose a two-dimensional (2-D) space-scale analysis of fringe patterns collected from a diffraction phase microscope based on the 2-D Morlet wavelet transform. We show that the adaptation of a ridge detection method with anisotropic 2-D Morlet mother wavelets is more efficient for analyzing cellular and high refractive index contrast objects than Fourier filtering methods since it can separate phase from intensity modulations. We compare the performance of this ridge detection method on theoretical and experimental images of polymer microbeads and experimental images collected from living myoblasts. [DOI: 10.1117/1.JBO.19.3.036007]

Keywords: quantitative phase imaging; diffraction phase microscopy; continuous wavelet transform; space-scale analysis; interferometry.

Paper 130776RR received Oct. 29, 2013; revised manuscript received Jan. 28, 2014; accepted for publication Jan. 30, 2014; published online Mar. 10, 2014.

1 Introduction

During the past century, the attraction of biophysicists for observing and characterizing living matter at cellular and subcellular levels has been the prime mover for developing sophisticated microscopic devices. Even if the concept of diffraction-limited imaging and interferometry principles[1] was established for a long time, the actual development of microscopic devices based on interferometric contrast was achieved in the first part of the 20th century by Zernike[2] and Nomarski and Weill[3] and further developed by Gabor,[4] who pioneered the principle of holographic microscopy. Retrieving a phase information from the light transmitted through transparent objects, like living cells, has benefited from the development of coherent sources, optoelectronic polarizing tools, and fast and sensible cameras in the second part of the 20th century. It is nowadays quite straightforward to design a compact, highly sensitive phase microscope that can follow in real time the dynamics of cells. In the last decade, different teams[5–13] have played a major role in disseminating the concepts of quantitative phase microscopy (QPM) among the optical and biophysical community. They have applied this technique to the real-time characterization of cellular dynamics and their alteration in cases of diseases.[6,13–16]

Other approaches that do not rely on interferometric principles have also been proposed to circumvent the constraint of high degree of coherence. They rather start from a principle of electromagnetic energy conservation, written as the divergence of the wave flow vector being equal to zero.[17–21] The technique of transport of intensity is valid only for weak defocus and reduces to a differential equation for field propagation.[22,23] This method is interesting for partially coherent illumination such as given by broadband polychromatic sources. For thick samples, three-dimensional computation is required.[24]

The principle of diffraction phase microscopy (DPM) introduced by Popescu and coauthors[25–27] relies on both off-axis and common-path principles in combination with fast acquisition rate and high temporal sensitivity. The interference patterns produced by a DPM system correspond to the superimposition of a simple carrier fringe pattern, given, for instance, by a diffraction grating, with the image of the object through the objective lens. To retrieve the phase image associated with the sample object, different methods have been proposed, including Hilbert transform followed by phase unwrapping,[28,29] derivative methods,[30] and Fourier filtering to avoid unwrapping problems.[31] All these phase retrieval algorithms rely on the assumption that the object phase does not alter the fringe carrier pattern, allowing a quasi one-dimensional analysis of interference patterns. To improve this approach and delineate more precisely the validity of this assumption, we propose here to generalize Fourier filtering methods using a two-dimensional (2-D) space-scale analysis based on Morlet wavelet transform.[32] We first introduce the DPM principle and illustrate it on simple physical objects, such as micron-size particles. We then describe the space-scale analysis and the possibility to measure directly the phase of the interference pattern from the detection of the ridges of the Morlet wavelet transform of the original image. Finally, we illustrate this method on living myoblasts, showing that both the modulus and the phase of the interference pattern can be retrieved.

*Address all correspondence to: Françoise Argoul, E-mail: fargoul@ens-lyon.fr

2 Modeling the QPM System Response and Its Space-Scale Analysis

Popescu and coauthors[25–27] designed an elegant QPM by introducing an amplitude diffraction grating in the image plane of an inverted microscope to generate multiple diffraction orders containing the full spatial information about the transparent object crossed by the light beam. This QPM setup, inspired from this principle, was assembled in our laboratory. It is described in the Sec. 7 and illustrated in Fig. 1. After the transmission grating G, the zeroth- (U_0) and first-order (U_1) components of the diffracted beams are separated in the conjugated Fourier plane of the image plane of the microscope. Then, the zeroth order is low-pass filtered with a spatial filter and recombined with the first order, thanks to a second Fourier lens L_2 to give a spatially modulated interference image $I(x,y)$ similar to the one shown in Fig. 2(a), captured from a glass coverslip covered by a scratched polymer layer. The vertical fringes of this image have a frequency f_g that is related to the grating period; they superimpose to the object phase image. We propose here a method based on a 2-D continuous wavelet transform (CWT) to retrieve the object phase information from this type of image.

The intensity map $I(x,y)$ recorded on the CMOS camera is directly proportional to the modulus square of the electric field at this point.

$$I(\vec{x}) = |U_0 + U_1|^2(\vec{x}) = [|U_0|^2 + |U_1|^2 + U_0U_1^* + U_0^*U_1](\vec{x}). \quad (1)$$

If f_g is the spatial frequency of the grating, the phase difference between U_1 and U_0 includes both the grating and the object phase information: $\Phi(\vec{x}) = f_g x + \phi(\vec{x})$, with $\vec{x} = (x,y)$. This gives a synthetic form of $I(\vec{x})$.

$$I(\vec{x}) = P(\vec{x}) + Q(\vec{x})\cos[f_g x + \phi(\vec{x})]. \quad (2)$$

$\phi(\vec{x})$ is the phase due to the object transmission at location $\vec{x}$. $P(\vec{x})$ and $Q(\vec{x})$ are real valued; they correspond, respectively, to the background and modulation intensities at location $\vec{x}$. One common assumption is that $P(\vec{x})$ and $Q(\vec{x})$ vary much slower than $\phi(\vec{x})$. The local frequencies of the signal U can be computed in both directions x and y from the partial derivatives of the phase $\phi(\vec{x})$.

$$f_x(\vec{x}) = f_g + \partial[\phi(\vec{x})]/\partial x, \quad (3)$$

$$f_y(\vec{x}) = \partial[\phi(\vec{x})]/\partial y. \quad (4)$$

These equations can be rewritten in the vectorial form.

$$\begin{bmatrix} f_x \\ f_y \end{bmatrix} = \vec{\nabla}[f_g x + \phi(\vec{x})]. \quad (5)$$

Equation (3) shows that the local frequency in x may deviate from the carrier frequency f_g depending on the strength of the phase derivative with respect to x, the steeper $\phi(\vec{x})$, the larger this deviation.

By a simple computation, assuming that we are characterizing a homogeneous object of thickness d and index n imbedded in a continuum medium of index n_0, we can approximate the optical path change Δp_o at the center of the object with the relation $\Delta p_o \sim d(n - n_0)$ and $\Delta\phi = 2\pi\Delta p_o/\lambda$. Assuming that the microscope can achieve a 10^{-2} rad phase sensitivity, this gives the possibility to detect objects of thickness $10^{-2}\lambda/(2\pi\Delta n)$, which for a refractive index drop of 0.2 and wavelength $\lambda = 532$ nm gives a sensitivity to objects with thickness down to 4 nm, along the optical axis.

The practical treatment of interference fringe patterns often assumes that the background and the fringe modulation intensities as well as the phase vary slowly across the fringe pattern.[33,34] This may no longer be true when the fringe pattern is produced by a highly diffracting object, such as a highly structured living cell, for instance, with thickness of several micrometers. A living cell is not a homogeneous medium, but is made of compartments surrounded by lipid membranes with high refractive index (plasmic membrane, nuclear membrane, Golgi apparatus, mitochondrial network) and highly dynamic proteic fiber network (cytoskeleton, nuclear matrix). This situation requires a method that is able to capture the spatial variation of the local frequencies f_x and f_y, without being biased by the spatial dependence of the fringe amplitude $Q(\vec{x})$ [Eq. (2)]. The wavelet transform offers this possibility since it allows a decomposition of a signal (uni- or multidimensional) into atoms

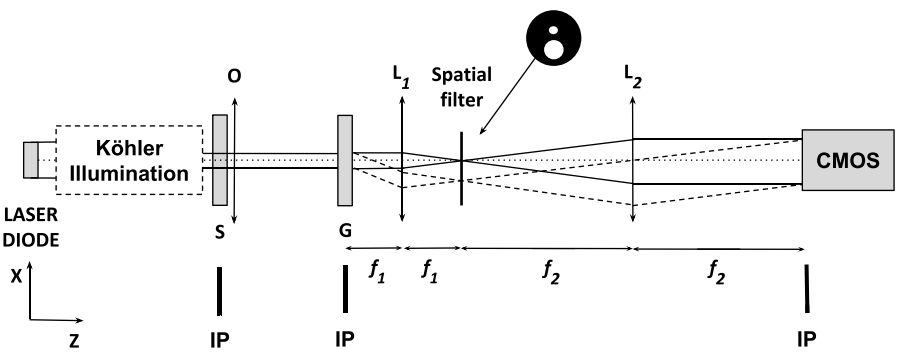

Fig. 1 Quantitative phase microscopy (QPM) setup. A transmission grating (G), positioned at the image plane (IP) of the microscope objective lens (O), is used for beam division into a central beam (order 0) and two symmetric beams (order 1) with respect to the optical axis. A spatial filter is placed at the Fourier plane of the lens L_1 to select the first-order beam (imaging field) and to low-pass filter the zeroth-order beam.[25–27] The two beams are recombined with the lens L_2 and the interferogram is recorded on a CMOS camera.

(wavelets) that are well localized in space and frequency.[35] The CWT is a mathematical technique introduced in signal analysis in the early 1980s.[36,37] Since then, it has been the subject of considerable theoretical developments and practical applications in a wide variety of fields.[38–54] An optical wavelet device has also been designed that performs the CWT, thanks to Fourier optics principles.[55,56] We choose here a 2-D Morlet wavelet[32] because it is particularly well suited for time (or space) frequency analysis.

3 Phase Map Reconstruction Using the CWT

Phase stepping and Fourier transform methods have been proposed in the 1980s for interferogram analysis in one and two dimensions.[33,57] These methods, however, assume that the coefficients $P(\vec{x})$ and $Q(\vec{x})$ vary slowly over one fringe cycle, so they can be treated as constants. To our knowledge, the first attempt to use a wavelet transform as a processing tool with white-light interferometry dates back to 1997.[58] Since then many teams have used this tool with success, in one dimension[59–67] as well as in two dimensions.[68–75]

More than a simple signal filtering tool, the wavelet transform analysis can also offer the possibility of a direct computation of the phase of the interferometry image, thanks to a wavelet transform ridge detection algorithm.[59–62,64,66,67,75]

The 2-D CWT of an interferogram $I(\vec{x})$ with $\vec{x} = (x, y)$ is defined as[52]

$$W_\Psi(\vec{b}, a, \theta) = a^\eta \int_{\Re^2} I(\vec{x}) \Psi^*[a^{-1} r_\theta(\vec{x} - \vec{b})] d^2\vec{x}. \quad (6)$$

$W_\Psi(\vec{b}, a, \theta)$ is the wavelet transform coefficient, at position $\vec{b}$, scale parameter a, and rotation angle θ. $\vec{b} = (b_x, b_y)$ is a 2-D translation parameter describing the position of the wavelet, $a > 0$ is the scale dilation parameter (nondimensioned), θ is a rotation parameter, $\mathbf{r}_\theta$ is the 2×2 rotation operator matrix, Ψ is the mother wavelet, Ψ^* is the complex conjugate of Ψ, and η is a normalization exponent. In Fourier space, the wavelet transform reads as

$$W_\Psi(\vec{b}, a, \theta) = a^\eta \int_{\Re^2} \hat{I}(\vec{k}) e^{i\vec{b}\cdot\vec{k}} \hat{\Psi}^*[a r_{-\theta}(\vec{k})] d^2\vec{x}. \quad (7)$$

The symbol $\hat{}$ denotes the Fourier transformation. A typical mother wavelet commonly used to detect localized and oriented features is the 2-D Morlet wavelet.[52]

$$\Psi_M(\vec{x}) = e^{i\vec{k}_0\cdot\vec{x}} e^{-\frac{1}{2}|A\vec{x}|^2} - e^{-\frac{1}{2}|A^{-1}\vec{k}_0|^2 - \frac{1}{2}|A\vec{x}|^2}, \quad (8)$$

$$\hat{\Psi}_M(\vec{k}) = \sqrt{\varepsilon}[e^{-\frac{1}{2}|A^{-1}(\vec{k}-\vec{k}_0)|^2} - e^{-\frac{1}{2}|A^{-1}\vec{k}_0|^2 - \frac{1}{2}|A^{-1}\vec{k}|^2}]. \quad (9)$$

The parameter k_0 is the wave vector and $A = diag[1, \varepsilon^{1/2}]$ is a 2×2 anisotropic matrix ($\varepsilon \geq 1$).

We use here this anisotropic 2-D continuous Morlet wavelet transform, with anisotropy factor ϵ, to extract the phase of a fringe pattern obtained with the QPM, such as shown in Fig. 2(a). The correction terms in Eqs. (8) and (9) enforce the admissibility condition $\hat{\Psi}_M(\vec{0}) = 0$. However, they are numerically negligible for $|k_0| \geq 5.6$, and one usually drops them. Putting $\varepsilon = 1$ and removing the correction terms gives the Gabor function.

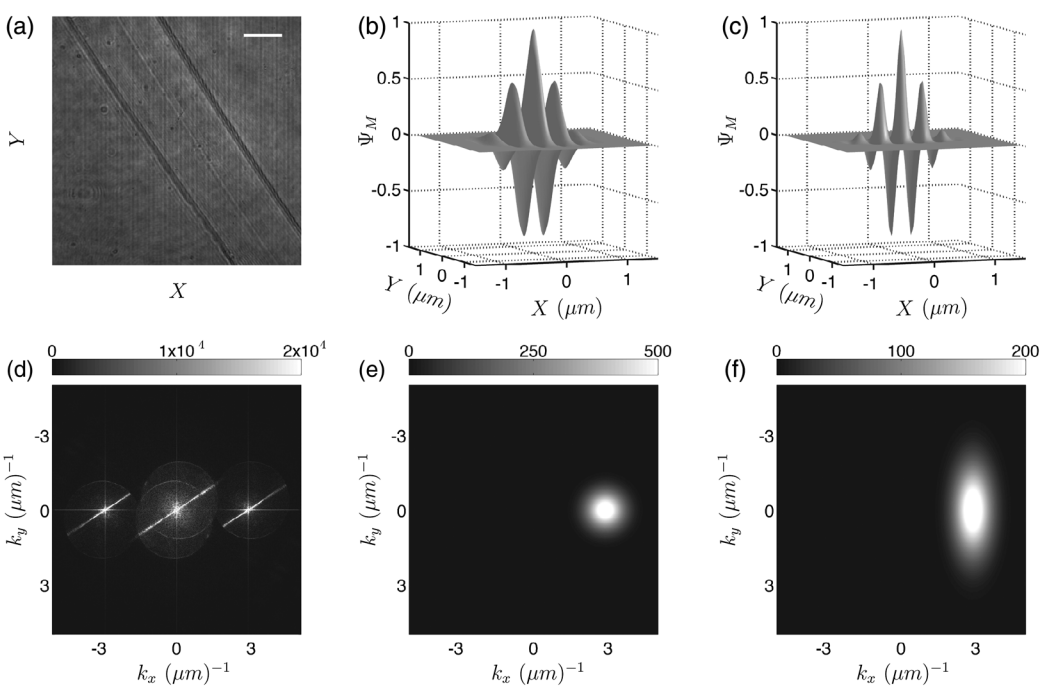

Fig. 2 (a) Untreated QPM image of a glass coverslip coated with polymer layer including a scratch in the diagonal direction. The scale bar is 10 μm. (b) Real part of the symmetric two-dimensional (2-D) Morlet wavelet Ψ_M with $\epsilon = 1$. (c) Real part of the anisotropic two-dimensional Morlet wavelet Ψ_M, with $\epsilon = 10$. (d), (e), and (f) modulus of the 2-D Fourier transforms of (a), (b), and (c), respectively, coded with a gray colormap.

$$\Psi_G(\vec{x}) = \exp(i\vec{k}_0 \cdot \vec{x}) \exp\left(-\frac{1}{2}|\vec{x}|^2\right). \tag{10}$$

The Morlet wavelet is a complex function; the modulus of the truncated Morlet wavelet (without the correction term) is a Gaussian, elongated in the x direction if $\varepsilon \geq 1$, and its phase is constant along the direction orthogonal to $\vec{k}_0$, and linear in $\vec{x}$, mod$(2\pi/|k_0|)$, along the direction of $\vec{k}_0$. As compared to the 1-D case, the additional feature of the 2-D Morlet (or Gabor) wavelet function is its inherent directivity, entirely contained in its phase. This turns to be a crucial advantage for studying objects with directional properties. Indeed, since the wavelet transform [Eq. (6)] is a convolution product of the fringe pattern with the dilated wavelet, we see that the wavelet transform smoothes the image in all directions, but detects the sharp transitions in the direction perpendicular to $\vec{k}_0$. In Fourier space, the effective support (footprint) of the function $\hat{\Psi}_M$ is an ellipse centered at $\vec{k}_0$ and elongated in the k_y direction. In Figs. 2(b) and 2(c) we show two Morlet wavelets computed for $\vec{k}_0 = (5.6, 0)$, and $\varepsilon = 1$ and $\varepsilon = 10$, respectively; their Fourier transforms are shown in Figs. 2(e) and 2(f). Since the ratio of the axes is equal to $\sqrt{\varepsilon}$, the cone of the wavelet in Fourier space elongates along k_y direction as ε increases. This wavelet preferentially detects edges perpendicular to the y-direction (i.e., parallel to $\vec{k}_0$), and its angular selectivity increases with k_0 and with the anisotropy ε. For the optical image shown in Fig. 2(a) recorded with the QPM from a glass coverslip coated with a scratched polymer layer, the best selectivity is achieved with $\vec{k}_0$ perpendicular to the long axis of the ellipse in $\vec{k} - space$, that is $\vec{k}_0 = (k_0, 0)$. We show in Fig. 2(d) the modulus of the Fourier transform of the fringe image shown in Fig. 2(a). The Morlet wavelet selects the right part of this Fourier transform by performing a band-pass filtering around the grating frequency. The advantage of taking a smooth wavelet and not a simply circular window in Fourier space[31] is not only to avoid the introduction of artificial oscillations produced by the sharp boundary of such a window, but also to have the ability to use the mathematical formalism of wavelet analysis, for instance, the ridge detection method.[52] The Morlet wavelet Ψ_M is then written as

$$\Psi_M(\vec{x}) = \exp\left[-\frac{1}{2}(x^2 + \varepsilon y^2)\right][\exp(ik_0 x) - \exp(-k_0^2/2)]. \tag{11}$$

We notice the general form of the truncated Morlet wavelet.

$$\Psi_M(\vec{x}) = V_\Psi(\vec{x}) \exp[i\phi_\Psi(\vec{x})], \qquad \phi_\Psi(\vec{x}) = k_0 x, \tag{12}$$

where $V_\Psi(\vec{x})$ is an anisotropic Gaussian function and ϕ_Ψ is the phase of the wavelet.

The ridge of the wavelet transform can be computed at each spatial point $\vec{x}$; it corresponds to a scale $a_r(\vec{b})$ such that the local derivative of the wavelet phase ϕ_Ψ compensates the local derivative of the object phase ϕ.

$$f_g \vec{\nabla}(x, 0) + \vec{\nabla}\phi(\vec{x}) - \vec{\nabla}\phi_\Psi[a_r^{-1}(\vec{b}) r_\theta(\vec{x} - \vec{b})] = 0. \tag{13}$$

If we consider only the modulated part of the fringe pattern $Q(\vec{x}) \exp[i\phi(\vec{x})]$ (complex form), we can derive the equation for its Morlet CWT, given that $Q(\vec{b})$ changes slowly compared to the phase of the fringes; the rotation angle is fixed, $\theta = 0$. It is important to note here that the choice of $\eta = 2$ (norm $\mathcal{L}^1$)[52,63,64,74] makes this computation straightforward.

$$W_\Psi(\vec{b}, a) = \frac{\hat{\Psi}_M\{a[f_g(1,0) + \vec{\nabla}\phi(\vec{b})]\}}{C(\vec{b}, a)} Q(\vec{b}) e^{i\phi(\vec{b})}, \tag{14}$$

up to a correction term $C(\vec{b}, a)$ that depends on the local variations of the phase $\phi(\vec{x})$ and the modulation amplitude $Q(\vec{x})$ of the optical signal on the ridge skeleton. Note that this correction term is constant in the approximation of a slow spatial variation $Q(\vec{b})$. Equation (14) is a local equation describing the shape of the wavelet transform in the vicinity of the scale $a_r(\vec{b})$ that maximizes its modulus; this shape is Gaussian because $\hat{\Psi}_M$ is a Gaussian function.

Hence, from Eq. (9), the maxima of the modulus of the CWT correspond to the wavelet ridge skeleton, where the optical phase ϕ produced by the object fulfills the equation

$$\vec{k}_0 / a_r(\vec{b}) = f_g(1, 0) + \vec{\nabla}\phi(\vec{b}). \tag{15}$$

It can be demonstrated analytically that this ridge detection method is independent of the modulation intensity $Q(\vec{x})$ [Eq. (2)] of the original fringe pattern (as long as the fringes are detectable) using the properties of Gaussian functions in real and Fourier spaces. This result can be intuitively understood because the ridge detection method boils down to the computation of the position of a local maxima of the wavelet transform with the scale parameter a, whatever the value of this maxima. The modulus of the wavelet transform on the ridge skeleton reads

$$W_\Psi[\vec{b}, a_r(\vec{b})] = \frac{\hat{\Psi}_M(\vec{k}_0)}{C[\vec{b}, a_r(\vec{b})]} Q(\vec{b}) e^{i\phi(\vec{b})}. \tag{16}$$

According to Eq. (16), we could straightforwardly compute $\phi(\vec{b})$ from the phase of the wavelet transform $W_\Psi[\vec{b}, a_r(\vec{b})]$, without using the derivative form of Eq. (15). This is not true when the variations of the phase and their amplitude modulations are too fast compared to f_g, giving a complex value to $C[\vec{b}, a_r(\vec{b})]$. In that case, Eq. (15) must be preferred. We also note that the modulus of the wavelet transform on the ridge follows the fringe amplitude modulation $Q(\vec{b})$. As a general remark, this wavelet-based method intrinsically eliminates background intensity variations $P(\vec{x})$ that do not affect the fringe pattern modulations.

4 Validation of the CWT Ridge Detection Method on Latex Microbeads

We discuss the efficiency of the 2-D CWT ridge detection method on a model system made of a microbead particle (radius $R = 5\ \mu$m) with refractive index $n_b = 1.59$ surrounded by a matching index oil $n_0 = 1.5167$. Figure 3(a) shows the fringe pattern computed with Eq. (2) for the 2-D phase of the bead.

$$\phi(\vec{x}) = [4\pi(n_b - n_0)\sqrt{R^2 - (\vec{x} - \vec{x}_c)^2}]/\lambda, \tag{17}$$

where $\vec{x}_c$ corresponds to the projection of the center of the bead in the (X, Y) plane. This bead is a good model of the experimental fringe patterns that will be presented later on. It is a good guide for defining the optimum wavelet parameters for

retrieving the phase from a fringe pattern. We observe in Fig. 3 (a) that on the border of the bead there is a breakdown of the fringe continuity because the phase derivative is not continuous at these points, which makes the phase computation harder. Figures 3(b) and 3(c) [respectively, Figs. 3(d) and 3(e)] show a gray-coded representation of the modulus of the 2-D CWT on the horizontal (respectively, vertical) section shown in Fig. 3(a). The 2-D CWT of the horizontal section [Figs. 3(b) and 3(c)] shows a strong deformation of the ridge $a_r(b_x)$ when entering and exiting the bead. This is also visible on the fringe pattern [Fig. 3(a)] since on the left side of the bead the fringes are compressed (smaller scale a), whereas on the right side they are dilated (larger scale a). Close to the border of the bead, $|W_\Psi(.,a)|$ is no longer a single humped Gaussian function (reflecting the shape of the modulus of the wavelet) since two maxima appear, corresponding to the existence of two local frequencies slightly splitted apart from the carrier fringe frequency f_g, corresponding to $a=1$ here. When the anisotropy of the 2-D Morlet wavelet is increased [see Fig. 3(c)], the ridge detection is more acurate, improving the detection of the border of the bead. The improvement provided by an anisotropic wavelet is more visible on the 2-D CWT analysis of a vertical section, shown in Figs. 3(d) and 3(e). $|W_\Psi(b_y,a)|$ keeps its single humped shape, except in a close neighborhood of the bead border, where it vanishes. This evanescence of the $|W_\Psi(.,a)|$ curves prevents a precise determination of the scale a_r where it is maximum. With an anisotropic 2-D Morlet wavelet ($\epsilon=10$), this vanishing is more localized in b_y and damped [Fig. 3(e)]. The evanescence of the wavelet transform modulus maxima curves is explained by a rapid shift of the fringes along the axis X and their summation by the wavelet transform, since its width is ~5.6 fringe periods along X. The 2-D CWT with a Morlet analyzing wavelet is, therefore, particularly suited for the detection of fringe compression or dilation along the X direction. It is less efficient to detect the shift of fringes along X, especially with curved fringes. From this 2-D CWT analysis, we can propose three methods for phase retrieval.

- 1. The first method uses the 2-D Morlet wavelet as a Fourier filter, with a fixed scale $a=1$ corresponding to the grating fringe modulation f_g; it does not use the ridge detection. We will call it the Fourier filtering method 1.
- 2. The second method uses the 2-D CWT ridge detection method to compute the phase derivative of the fringe pattern, described by Eq. (15), and makes an integration of this derivative along X. We will call it the ridge integral method 2.
- 3. The third method uses the 2-D CWT ridge detection method to compute the new complex quantity $W_\Psi[b,a_r(\vec{b})]$ on the ridge and takes its argument to compute the phase [Eq. (16)]. We will call it the ridge argument method 3.

Figure 4 compares these three methods for phase retrieval on the bead model, for two values of the anisotropy factor ϵ. Figures 4(a) and 4(b) show the phase extracted with a simple Fourier filtering of the fringe pattern, using a Morlet wavelet at fixed scale a. This method does not succeed to recover the theoretical phase whatever ϵ because on the border of the bead, the local frequency of the fringes is too far from the fringe carrier f_g, and it is, therefore, impossible to estimate their phase correctly. Figures 4(c) and 4(d) show the ridge integral method 2 on this bead model. In that case, the theoretical phase can be estimated correctly on the central part of the bead, but computation errors remain on the top and bottom borders of the bead, which come from the difficulty to capture the local CWT modulus maxima position when this modulus vanishes. With method 2, the phase is computed by integration of the gradient $\vec{\nabla}\phi(\vec{b})$ along the axis b_x, which produces an accumulation of the errors on $\phi(\vec{x})$ on the right side of the bead. However, switching from isotropic [Fig. 4(c) and $\epsilon=1$] to anisotropic wavelet [Fig. 4(d) and $\epsilon=10$] corrects the errors on the top and the bottom borders of the bead, but the integration errors remain. To improve this aspect, a higher resolution in the modulus maxima detection method is necessary at the expense of computation time. Note, however, that if the fringe pattern is very noisy, method 2 avoids the unwrapping of the phase and may stabilize the computation of the phase. Figures 4(e) and 4(f) show the ridge argument method 3. This method is still sensitive to fringe discontinuities [Fig. 4(e)] on the top and the bottom borders of

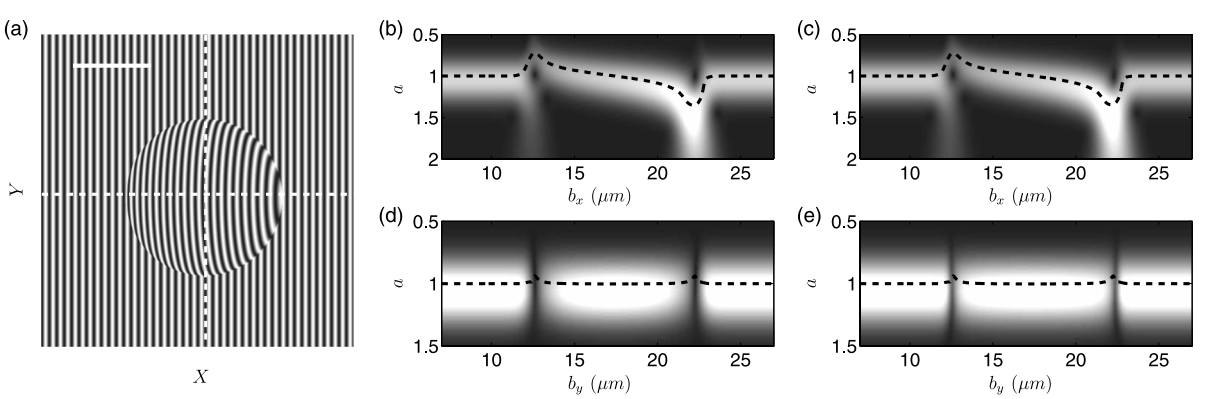

Fig. 3 (a) Theoretical QPM intensity image of a transparent micro-bead, computed with Eqs. (2) and (17). The scale bar is 5 μm. (b) and (d) Modulus of the 2-D continuous wavelet transform (CWT) on the horizontal (fixed Y) section shown in (a) by a white dashed line. (c) and (e) Modulus of the 2-D CWT on the vertical (fixed X) section shown in (a) by a white dashed line. (b) and (d) have been computed with an isotropic 2-D Morlet wavelet ($\epsilon=1$). (c) and (e) have been computed with an anisotropic 2-D Morlet wavelet ($\epsilon=10$). $a=1$ corresponds to the fringe frequency f_g. The dashed black lines outline the $a_r(\vec{b})$ ridge functions. The gray coding is identical for all CWT modulus images, from zero (black) to 0.8 (white).

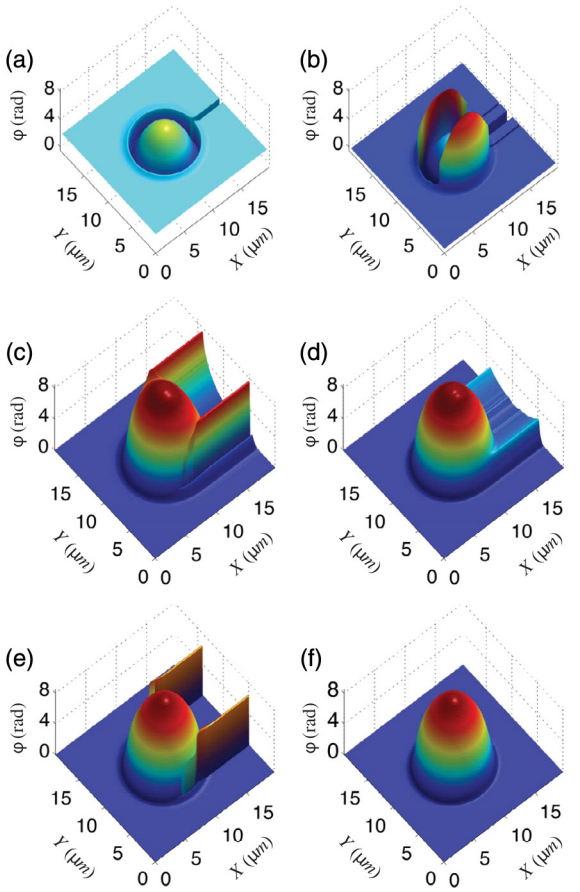

Fig. 4 Three-dimensional (3-D) representation of the reconstructed phases from the fringe pattern of Fig. 3(a) with methods 1 [(a) and (b)], 2 [(c) and (d)], and 3 [(e) and (f)]. (a), (c), and (e) are computed with the isotropic Morlet wavelet ($\epsilon = 1$). (b), (d), and (f) are computed with the anisotropic Morlet wavelet ($\epsilon = 10$). The phase ϕ is given in radians.

the bead. With an anisotropic wavelet ($\epsilon = 10$), this method succeeds to reproduce the theoretical phase with a 10^{-3} relative error on the phase. The possibility to adjust the anisotropy of the wavelet is, therefore, important for analyzing phase discontinuities; it has never been reported in that context.

To compare with the bead model, we have imaged a 5 μm radius latex microbead with the QPM and applied the 2-D anisotropic CWT ($\epsilon = 10$) to analyze the experimental fringe pattern shown in Fig. 5(a). Unlike the theoretical model, the fringe intensity modulation in the QPM is no longer constant, see the horizontal section plotted in black in Fig. 5(b). This intensity modulation is produced by the light scattering by the bead. As established by Bedrosian,[76] when this modulation contains frequencies that overlap with the fringe carrier frequency f_g, the extraction of the phase with the Hilbert method is biased and leads to a false estimation. Indeed, from the Hilbert transform of the term $Q(\vec{x})\cos[f_g x + \phi(\vec{x})]$ in Eq. (2), we would like to recover a function like $Q(\vec{x})\sin[f_g x + \phi(\vec{x})]$ from which the phase could be computed straightforwardly. Bedrosian's theorem shows that this is workable only if the amplitude modulation $Q(\vec{x})$ does not contain frequencies that mix with the carrier frequency f_g. This condition is not experimentally satisfied as illustrated in Fig. 5(b). In that case, when using the ridge detection, the CWT offers the advantage of leading to a measure of the frequency from the ridge that considerably reduces the effects of fringe modulation amplitude on phase retrieval [Eq. (15)]. In Fig. 5(c), we show the modulus of the 2-D CWT $|W_\Psi(b_x, a)|$ on the horizontal section shown in Fig. 5(a). The ridge $a_r(\vec{b})$ plotted in Fig. 5(c) with a black line is very similar to the theoretical curve shown in Fig. 3(c). The real part of the CWT computed on the ridge shown in Fig. 5(d) is very impressive when compared to the original image [Fig. 5(a)]. It looks as if the major intensity modulations of the original images were damped out to keep only the fringe distorsion, from which the phase is computed. The same section of Fig. 5(d) is plotted in gray in Fig. 5(b). The efficiency of the wavelet transform is well illustrated in this example. Figure 5(e) shows the modulus $|W_\Psi[\vec{b}, a_r(\vec{b})]|$ computed on the ridge of the 2-D CWT on this latex microbead; it is coded in gray from minimum (black) to maximum (white). Figure 5(f) gives a 2-D gray-coded image of the phase derivative $\partial\phi(\vec{b})/\partial b$ of the CWT on the ridge, and Fig. 5(g) shows the three-dimensional (3-D) representation of the phase $\phi(\vec{x})$ computed from the ridge of the CWT with method 3. The modulus of the 2-D CWT on the ridge preserves the intensity of the original fringe image, whereas this intensity modulation disappears completely on the phase derivative $\partial\phi(\vec{b})/\partial b$. We also note that as for the bead model, the anisotropic Morlet wavelet allows a very nice detection of the phase derivative. The 3-D picture of the phase in Fig. 5(g) is very appealing since it not only detects perfectly the phase drop due to this bead and reproduces the theoretical prediction, but also delineates some defects of the beads that are visible as phase irregularities on the surface of the bead. We have estimated the standard deviation of the background phase on this image of ~0.25 rad.

5 Application of the CWT Phase Retrieval Method to Living Cell Imaging

We illustrate the performance of the CWT phase retrieval method on a murine myoblast cell line C2C12, which can be differentiated to give rise to plurinucleate syncytia (the myotubes) by fusion. We will focus here on undifferentiated C2C12 cell monolayers. Figure 6 reports the 2-D CWT ridge analysis of a QPM image of a nonadherent myoblast that is progressively rounding and will detach from the glass to enter mitosis.[77] The characteristic organization of the microtubule-actin cytoskeleton with stress fibers has disappeared, the cell is round, and it is no longer possible to delineate a nice nuclear contour inside this cell. However, this spherical shape is interesting because it allows us to perform the same parametrization of the phase map as we have done previously for spherical particles. Compared to the previous example of the microbead in Sec. 4, we observe on Fig. 6(a) that besides scattering effects on the border of the bead, the internal structure of the cell also produces intensity modulations of the fringes that may make the analysis more complex. We have plotted in Fig. 6(b) a profile of the fringe image selected on the white dashed section of Fig. 6(a) (black curve), which can be compared to the corresponding profile of the real part of the 2-D CWT ridge on the same section. Similar to the example of Fig. 5, the CWT ridge analysis regularizes the fringe intensity modulation. Figure 6(c) reports the modulus of the 2-D CWT $|W_\Psi(b_x, a)|$ on the horizontal section shown in Fig. 6(a). The ridge $a_r(\vec{b})$ plotted in Fig. 6(c) with a black line is reminiscent of the one shown in Fig. 5(c). The real part of the CWT computed on the ridge shown in Fig. 6(d) when compared to the original QPM image [Fig. 6(a)] definitely flattens the intensity

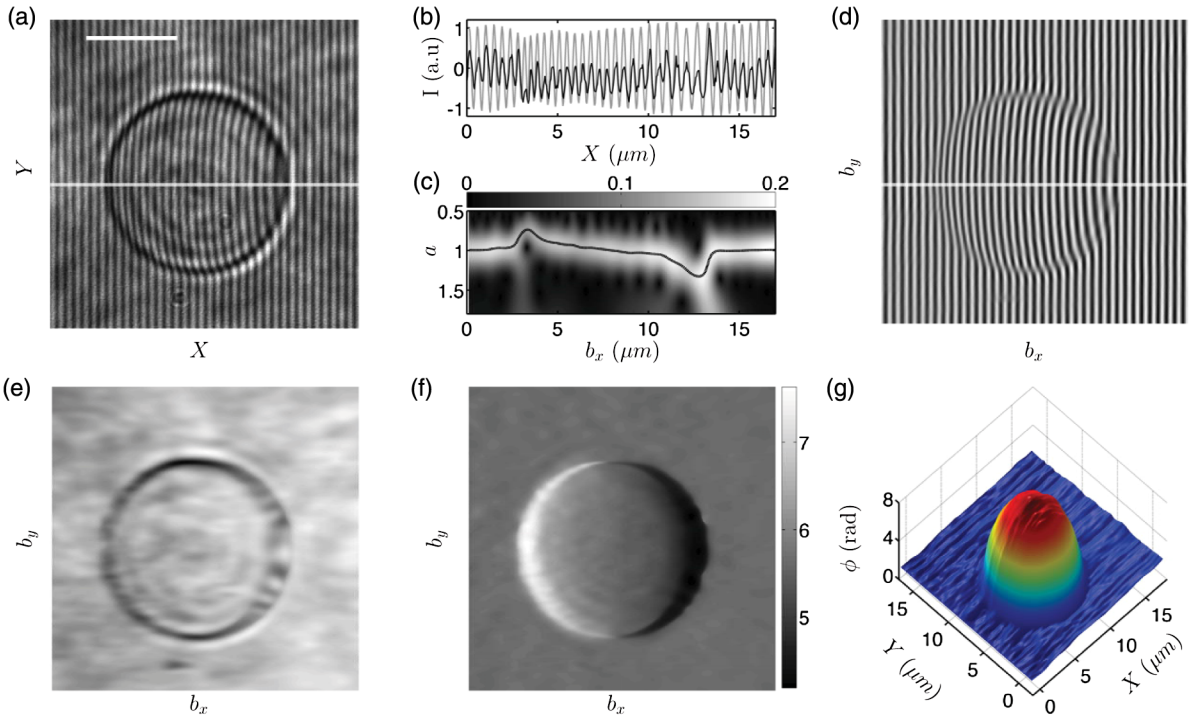

Fig. 5 2-D CWT analysis of an experimental QPM fringe pattern captured from a 5 μm radius latex microbead embedded in glass index matching oil. (a) The untreated QPM image. The scale bar is 5 μm. (b) Intensity profile (black line) of the section marked with a white dashed line in (a). The gray line corresponds to the real part of the CWT ridge computed on this section. (c) Gray coded modulus of the 2-D CWT on the horizontal section shown in (a). The ridge $a_r(\vec{b})$ is plotted with a black line. (d) Real part of the CWT computed on the ridge. (e) Modulus of the 2-D CWT computed on the ridge. (f) $\partial\phi(b)/\partial x$ computed from the ridge [Eq. (15)]. (g) 3-D representation of phase computed from the fringe pattern of (a) with method 3. The anisotropic Morlet wavelet ($\epsilon = 10$) is used for this analysis. The gray coding is done from black (minimum) to white (maximum).

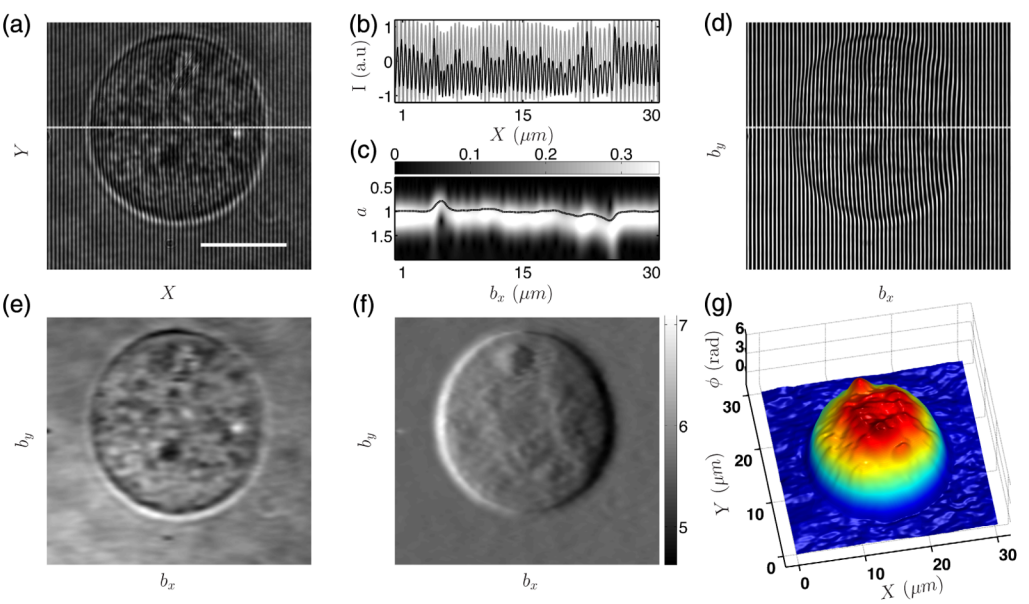

Fig. 6 2-D CWT analysis of a QPM fringe pattern collected from a round myoblast. (a) The untreated QPM image. The scale bar is 10 μm. (b) Intensity profile (black line) of the section marked with a white dashed line in (a). The gray line corresponds to the real part of the CWT ridge computed on this section. (c) Gray coded modulus of the 2-D CWT on the horizontal section shown in (a). The ridge $a_r(\vec{b})$ is plotted with a black line. (d) Real part of the CWT computed on the ridge. (e) Modulus of the CWT computed on the ridge. (f) $\partial\phi(b)/\partial x$ computed from the ridge of the CWT. (g) 3-D representation of phase computed from the fringe pattern shown in (a) with method 3. The anisotropic Morlet wavelet ($\epsilon = 10$) is used for this analysis. The gray coding is done from black (minimum) to white (maximum).

modulations. Figure 6(e) shows the modulus $|W_\Psi[\vec{b}, a_r(\vec{b})]|$ computed on the ridge of 2-D CWT; it is coded in gray from minimum (black) to maximum (white). The intensity modulation that remains in Fig. 6(e) is eliminated in the derivative of the phase shown in Fig. 6(f) (ridge method 2). Finally, using method 3, we reconstruct a 3-D profile of the phase of this myoblast in Fig. 6(g). This representation confirms the round shape of this cell in the third direction Z and points out a central part where smaller objects are identified, which may be attributed to condensed chromosomes. We use the same model as proposed for a spherical bead as a first approximation to extract the mean refractive index of this cell and delineate one of the protruding object and its refractive index. The interpolation of the whole cell by a spherical phase shape [Eq. (17)] is reported in Fig. 7. This interpolation leads to an estimation of the overall refractive index of the cell as $n_c = 1.36 \pm 0.005$, given that the buffer refractive index is $n_0 = 1.33$. Moreover, subtracting this mean spherical phase contour from the total phase contour (see Fig. 7), we can also compute the phase drop of the small spherical object that pops up on the upper part of the cell and estimate its index to be 1.4 ± 0.005.

In Fig. 8, we show the image of an adherent myoblast cell, where we can recognize thin lamellipodia extensions that exhibit filopodia projections on the leading edge: a characteristic pattern of cell motility. It has been shown in the literature that differentiation and fusion of myoblasts into multinucleated myotubes is accompanied by a dramatic reorganization of the Golgi complex.[78] Here we rather have the classic compact juxtanuclear Golgi complex of an undifferentiated myoblast that we can recognize as small granular objects on both the derivative of the phase ϕ reported in Fig. 8(c) and on the phase ϕ shown in a 3-D representation in Fig. 8(d). The phase response of this adherent cell is different from that shown for the round cell [Fig. 6(g)]; the nucleus looks more like a phase plateau, flattened by the mechanical tractions of the lamellipodia. On the border of the nucleus, the QPM detects a necklace of phase droplets and a central part with higher phase [Figs. 8(c) and 8(d)]. At this stage, it is difficult to conclude if these small bodies are essentially Golgi complex or a combination of perinuclear organelles as rough and smooth endoplasmic reticulum, Golgi, vesicles, and mitochondrial network.

6 Summary

We have shown that a wavelet-based space-scale analysis can be used to decode the fringe images recorded from living cells with a QPM. The implementation of the ridge detection method is more successful than Fourier filtering methods when imaging cellular and high refractive index contrast objects since it can discriminate intensity from phase changes. This technique has been applied to undifferentiated myoblast cells and revealed internal structures of these cells, which were confirmed by fluorescence imaging. This microscope is coupled to a high-speed camera, and we hope in the near future that besides capturing the optical phase changes produced by the cell internal structures, the record of the dynamics of these internal bodies will provide a complementary way to distinguish these structures without the need of fluorescence staining.

7 Materials and Methods

7.1 *Quantitative Phase Microscope*

A low-coherence laser diode (Thorlabs, GmbH, Germany, $\lambda = 532$ nm) is used as a light source and is directed to the sample (S) using Köhler illumination, such that the field at the image plane (IP) is spatially coherent over the entire field of view (Fig. 1). Different diffraction orders are then created with a transmission grating (G) (70 grooves/mm) localized at the IP of the microscope equipped with an objective (O) 40× (Olympus, France, SPlan40, N.A. = 0.7). A spatial filter (Thorlabs, custom-made) is placed at the Fourier plane of lens L_1 to select the first-order beam (imaging field) and to low-pass filter the zeroth-order beam (reference). The spatial filter has been designed with two circular apertures with diameters of 15 μm and 2 mm. The two beams are recombined using a second Fourier lens (L_2), and the resulting interferogram is recorded as an image of 2048 × 2048 pixels with a CMOS camera (Hamamatsu, Japan, ORCA-Flash 4.0). The $4f$ lens system adds a 5× magnification ($f_1 = 50$ nm, $f_2 = 250$ mm).

7.2 *Polymer Layer Preparation*

A solution of 10% poly(methyl methacrylate) (PMMA, Sigma-Aldrich, France) in toluene was spin coated over a glass coverslip at a speed of 1000 rpm during 50 s. A time of 10 s is fixed to reach the nominal speed. After coating, the film was annealed for 1 h at 140°C. Prior to imaging, a portion of the PMMA layer was removed with a scalpel.

7.3 *Polystyrene Beads Preparation*

1 μL of an aqueous solution containing polystyrene beads (FLUKA 72986) was diluted in 10 mL of deionized water.

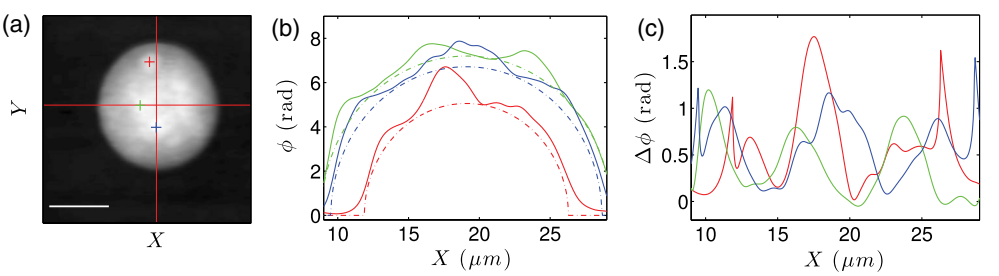

Fig. 7 Decomposition into spherical phase shapes of the myoblast phase map shown in Fig. 6. (a) The original 2-D phase map computed from the fringe pattern with ridge method 3. The gray coding is done from black (minimum) to white (maximum). (b) Horizontal sections corresponding to the colored crosses shown in (a) and their spherical phase contour envelope [Eq. (17)] in dashed line. (c) The subtraction of the original phase map with the spherical phase contour envelopes, revealing other phase contours of smaller objects, inside the cell. The red curve can again be parametrized by a spherical phase contour to estimate the index of this small protruding object, marked with a red cross in (a).

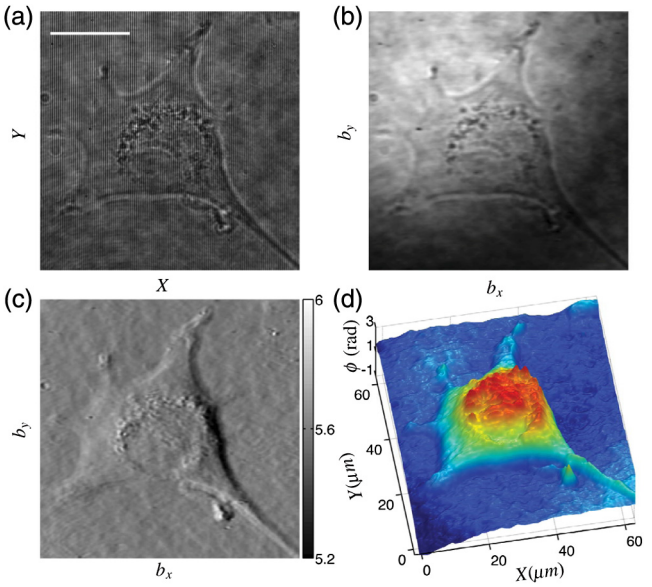

Fig. 8 2-D CWT analysis of a QPM fringe pattern collected from an adherent myoblast. (a) The untreated QPM image. The scale bar is 20 μm. (b) Modulus of the CWT computed on the ridge. (c) $\partial\phi(\vec{b})/\partial x$. (d) 3-D representation of phase computed from the fringe pattern in (a) with method 3. The anisotropic Morlet wavelet ($\epsilon = 10$) is used for this analysis. The gray coding is done from black (minimum) to white (maximum).

250 μL of the dilution were deposited on a small petri dish with a glass window and let overnight in an oven at 70°C to dry. Before imaging, 500 μL of glass index matching oil were added.

7.4 *Cell Culture*

C2C12 mouse cells (ATCC number CRL-1772™) were grown in high glucose (4.5 g/L) Dulbecco's modified Eagle medium [(DMEM), GE Healthcare Life Science, Dominique Dutscher, France] supplemented with 20% fetal bovine serum GE Healthcare Life Science and 1% antibiotics (penicillin/streptamicine). Adherent myoblasts on 50 mm petri dishes with a glass bottom of 0.17 mm thickness were maintained at 37°C and 5% CO_2 up to 60% confluence until they were used. The glass surface was not treated to enhance cell adhesion. The growth medium was replaced by phosphate buffered saline solution before imaging. No further sample preparation was required.

Acknowledgments

We are indebted to Centre National de la Recherche Scientifique, Ecole Normale Supérieure de Lyon, Lyon Science Transfert (projet L659), Région Rhône Alpes (CIBLE Program 2011), INSERM (AAP Physique Cancer 2012), and the French Agency for Research (ANR-AA-PPPP-005, EMMA 2011) for their financial support. C.M.T. is very grateful to the National Council of Science and Technology (CONACyT, Mexico) for supporting her PhD scholarship. L.S. is very thankful to the Association Française Contre les Myopathies, AFM-Téléthon, for supporting her PhD scholarship.

References

1. M. Born and E. Wolf, *Principles of Optics: Electromagnetic Theory of Propagation, Interference and Diffraction of Light*, 7th ed., Cambridge University Press, Cambridge (1999).
2. F. Zernike, "How I discovered phase contrast," *Science* **121**(3141), 345–349 (1955).
3. G. Nomarski and A. R. Weill, "Application à la métallographie des méthodes interférentielles à deux ondes polarisées," *Revue de Métallurgie* **2**, 121–128 (1955).
4. A. D. Gabor, "Microscopy by reconstructed wave-fronts," *Proc. R. Soc. Lon. A* **197**(1051), 454–487 (1949).
5. B. Rappaz et al., "Measurement of the integral refractive index and dynamic cell morphometry of living cells with digital holographic microscopy," *Opt. Express* **13**(23), 9361–9373 (2005).
6. L. Yu et al., "Digital holographic microscopy for quantitative cell dynamic evaluation during laser microsurgery," *Opt. Express* **17**(14), 12031–12038 (2009).
7. V. P. Tychinsky and A. N. Tikhonov, "Interference microscopy in cell biophysics. 1. Principles and methodological aspects of coherent phase microscopy," *Cell Biochem. Biophys.* **58**(3), 107–116 (2010).
8. G. Popescu, *Quantitative Phase Imaging of Cells and Tissues*, McGraw Hill, New York (2011).
9. N. Cardenas, S. Kumar, and S. Mohanty, "Dynamics of cellular response to hypotonic stimulation revealed by quantitative phase microscopy and multi-fractal detrended fluctuation analysis," *Appl. Phys. Lett.* **101**(20), 203702 (2012).
10. N. T. Shaked, "Quantitative phase microscopy of biological samples using a portable interferometer," *Opt. Lett.* **37**(11), 2016–2018 (2012).
11. N. Sugiyama et al., "Label-free characterization of living human induced pluripotent stem cells by subcellular topographic imaging technique using full-field quantitative phase microscopy coupled with interference reflection microscopy," *Biomed. Opt. Express* **3**(9), 2175–2183 (2012).
12. P. Bon, B. Wattellier, and S. Monneret, "Modeling quantitative phase image formation under tilted illuminations," *Opt. Lett.* **37**(10), 1718–1720 (2012).
13. P. Bon et al., "Optical detection and measurement of living cell morphometric features with single-shot quantitative phase microscopy," *J. Biomed. Opt.* **17**(7), 076004 (2012).
14. V. Tychinsky, "The metabolic component of cellular refractivity and its importance for optical cytometry," *J. Biophotonics* **2**(8–9), 494–504 (2009).
15. Y. Park et al., "Measurement of red blood cell mechanics during morphological changes," *Proc. Natl. Acad. Sci. U. S. A.* **107**(15), 6731–6836 (2010).
16. Y. Park et al., "Metabolic remodeling of the human red blood cell membrane," *Proc. Natl. Acad. Sci. U. S. A.* **107**(4), 1289–1294 (2010).
17. T. E. Gureyev, A. Roberts, and K. A. Nugent, "Phase retrieval with the transport-of-intensity equation: matrix solution with use of Zernike polynomials," *J. Opt. Soc. Am. A* **12**(9), 1932–1941 (1995).
18. T. E. Gureyev, A. Roberts, and K. A. Nugent, "Partially coherent fields, the transport-of-intensity equation, and phase uniqueness," *J. Opt. Soc. Am. A* **12**(9), 1942–1946 (1995).
19. S. Bajt et al., "Quantitative phase-sensitive imaging in a transmission electron microscope," *Ultramicroscopy* **83**(1–2), 67–73 (2000).
20. M. R. Teague, "Image formation in terms of the transport equation," *J. Opt. Soc. Am. A* **2**(11), 2019–2026 (1985).
21. G. Ade, "On the validity of the transport equation for the intensity in optics," *Opt. Commun.* **52**(5), 307–310 (1985).
22. M. Beleggia et al., "On the transport of intensity technique for phase retrieval," *Ultramicroscopy* **102**(1), 37–49 (2004).
23. A. Barty et al., "Quantitative optical phase microscopy," *Opt. Lett.* **23**(11), 817–819 (1998).
24. C. J. Bellair et al., "Quantitative phase amplitude microscopy IV: imaging thick specimens," *J. Microsc.* **214**(Pt 1), 62–69 (2004).
25. G. Popescu et al., "Diffraction phase microscopy for quantifying cell structure and dynamics," *Opt. Lett.* **31**(6), 775–777 (2006).
26. Y. Park et al., "Diffraction phase and fluorescence microscopy," *Opt. Express* **14**(18), 8263–8268 (2006).
27. B. Bhaduri et al., "Diffraction phase microscopy with white light," *Opt. Lett.* **37**(6), 1094–1096 (2012).
28. T. Ikeda et al., "Hilbert phase microscopy for investigating fast dynamics in transparent systems," *Opt. Lett.* **30**(10), 1165–1167 (2005).

29. H. V. Pham et al., "Real time blood testing using quantitative phase imaging," *PloS One* **8**(2), e55676 (2013).
30. B. Bhaduri and G. Popescu, "Derivative method for phase retrieval in off-axis quantitative phase imaging," *Opt. Lett.* **37**(11), 1868–1870 (2012).
31. H. V. Pham et al., "Fast phase reconstruction in white light diffraction phase microscopy," *Appl. Opt.* **52**(1), A97–101 (2013).
32. J. Morlet et al., "Wave propagation and sampling theory—Part II: Sampling theory and complex waves," *Geophysics* **47**(2), 222–236 (1982).
33. M. Takeda, H. Ina, and S. Kobayashi, "Fourier-transform method of fringe-pattern analysis for computer-based topography and interferometry," *J. Opt. Soc. Am.* **72**(1), 156–160 (1982).
34. C. Roddier and F. Roddier, "Interferogram analysis using Fourier transform techniques," *Appl. Opt.* **26**(9), 1668–16673 (1987).
35. P. Flandrin, *Time-Frequency / Time-Scale Analysis*, Academic Press, New York (1999).
36. P. Goupillaud, A. Grossmann, and J. Morlet, "Cycle-octave and related transforms in seismic signal analysis," *Geoexploration* **23**(1), 85–102 (1984).
37. A. Grossmann and J. Morlet, "Decomposition of Hardy functions into square integrable wavelets of constant shape," *SIAM J. Math. Anal.* **15**(4), 723–736 (1984).
38. J. M. Combes, A. Grossmann, and P. Tchamitchian, Eds., *Wavelets*, Springer, Berlin (1989).
39. I. Daubechies, *Ten Lecture on Wavelets*, SIAM, Philadelphia (1992).
40. Y. Meyer, Ed., *Wavelets and Their Applications*, Springer, Berlin (1992).
41. M. B. Ruskai et al., Eds., *Wavelets and Their Applications*, Jones and Bartlett, Boston (1992).
42. P. Flandrin, *Temps-Fréquence*, Hermès, Paris (1993).
43. Y. Meyer and S. Roques, Eds., *Progress in Wavelets Analysis and Applications*, Editions Frontières, Gif-sur-Yvette (1993).
44. A. Arneodo et al., *Ondelettes, Multifractales et Turbulences: de l'ADN aux croissances cristallines*, Diderot Editeur, Art et Sciences, Paris (1995).
45. A. Arneodo, E. Bacry, and J. F. Muzy, "The thermodynamics of fractals revisited with wavelets," *Physica A* **213**(1–2), 232–275 (1995).
46. G. Erlebacher, M. Y. Hussaini, and L. M. Jameson, Eds., *Wavelets: Theory and Applications*, Oxford University Press, Oxford (1996).
47. S. Mallat, *A Wavelet Tour of Signal Processing*, Academic Press, New York (1998).
48. B. Torresani, *Analyse Continue par Ondelettes*, Editions de Physique, Les Ulis (1998).
49. A. Arneodo, N. Decoster, and S. Roux, "A wavelet-based method for multifractal image analysis. I. Methodology and test applications on isotropic and anisotropic random rough surfaces," *Eur. Phys. J. B* **15**(3), 567–600 (2000).
50. A. Arneodo et al., "A wavelet-based method for multifractal image analysis: from theoretical concepts to experimental applications," *Adv. Imaging Electron Phys.* **126**, 1–92 (2003).
51. P. Kestener and A. Arneodo, "Generalizing the wavelet-based multifractal formalism to random vector fields: application to three-dimensional turbulence velocity and vorticity data," *Phys. Rev. Lett.* **93**(4), 044501 (2004).
52. J. P. Antoine et al., *Two-Dimensional Wavelets and Their Relatives*, Cambridge University Press, Cambridge, United Kingdom (2004).
53. A. Arneodo, B. Audit, and P. Kestener, "Wavelet-based multifractal analysis," *Scholarpedia* **3**(3), 4103 (2008).
54. A. Arneodo et al., "Multi-scale coding of genomic information: from DNA sequence to genome structure and function," *Phys. Rep.* **498**(2–3), 45–188 (2011).
55. E. Freysz et al., "Optical wavelet transform of fractal aggregates," *Phys. Rev. Lett.* **64**(7), 745–748 (1990).
56. J. F. Muzy et al., "Optical-diffraction measurement of fractal dimensions and $f(\alpha)$ spectrum," *Phys. Rev. A* **45**(12), 8961–8964 (1992).
57. W. W. Macy, "Two-dimensional fringe-pattern analysis," *Appl. Opt.* **22**(23), 3898–3901 (1983).
58. P. Sandoz, "Wavelet transform as a processing tool in white-light interferometry," *Opt. Lett.* **22**(14), 1065–1067 (1997).
59. P. Tomassini et al., "Analyzing laser plasma interferograms with a continuous wavelet transform ridge extraction technique: the method," *Appl. Opt.* **40**(35), 6561–6568 (2001).
60. J. Zhong and J. Weng, "Spatial carrier-fringe pattern analysis by means of wavelet transform: wavelet transform profilometry," *Appl. Opt.* **43**(26), 4993–4998 (2004).
61. H. Liu, "Experimental verification of improvement of phase shifting Moiré interferometry using wavelet-based image processing," *Opt. Eng.* **43**(5), 1206–1214 (2004).
62. J. Zhong and J. Weng, "Phase retrieval of optical fringe pattern from the ridge of a wavelet transform," *Opt. Lett.* **30**(19), 2560–2562 (2005).
63. Z. Wang and H. Ma, "Advanced continuous wavelet transform algorithm for digital interferogram analysis and processing," *Opt. Eng.* **45**(4), 045601 (2006).
64. S. Li, X. Su, and W. Chen, "Wavelet ridge techniques in optical fringe pattern analysis," *J. Opt. Soc. Am. A* **27**(6), 1245–1254 (2010).
65. M. A. Gdeisat et al., "Spatial and temporal carrier fringe pattern demodulation using the one-dimensional continuous wavelet transform: recent progress, challenges, and suggested developments," *Opt. Lasers Eng.* **47**(12), 1348–1361 (2009).
66. R. Oven, "Extraction of phase derivative data from interferometer images using a continuous wavelet transform to determine two-dimensional refractive index profiles," *Appl. Opt.* **49**(22), 4228–4236 (2010).
67. Z. Zhang et al., "Comparison of Fourier transform, windowed Fourier transform, and wavelet transform methods for phase calculation at discontinuities in fringe projection profilometry," *Opt. Lasers Eng.* **50**(8), 1152–1160 (2012).
68. M. A. Gdeisat, D. R. Burton, and M. J. Lalor, "Spatial carrier fringe pattern demodulation by use of a two-dimensional continuous wavelet transform," *Appl. Opt.* **45**(34), 8722–8732 (2006).
69. Q. Kemao, "Two-dimensional windowed Fourier transform for fringe pattern analysis: principles, applications and implementations," *Opt. Lasers Eng.* **45**(2), 304–317 (2007).
70. A. Federico and G. H. Kaufmann, "Phase retrieval of singular scalar light fields using a two-dimensional directional wavelet transform and a spatial carrier," *Appl. Opt.* **47**(28), 5201–5207 (2008).
71. H. Niu, C. Quan, and C. Tay, "Phase retrieval of speckle fringe pattern with carriers using 2D wavelet transform," *Opt. Lasers Eng.* **47**(12), 1334–1339 (2009).
72. S. Li, X. Su, and W. Chen, "Spatial carrier fringe pattern phase demodulation by use of a two-dimensional real wavelet," *Appl. Opt.* **48**(36), 6893–6906 (2009).
73. K. Pokorski and K. Patorski, "Visualization of additive-type Moiré and time-average fringe patterns using the continuous wavelet transform," *Appl. Opt.* **49**(19), 3640–3651 (2010).
74. J. Ma et al., "Two-dimensional continuous wavelet transform for phase determination of complex interferograms," *Appl. Opt.* **50**(16), 2425–2430 (2011).
75. K. Pokorski and K. Patorski, "Separation of complex fringe patterns using two-dimensional continuous wavelet transform," *Appl. Opt.* **51**(35), 8433–8439 (2012).
76. E. Bedrosian, "Product theorem for Hilbert transforms," *Proc. IEEE* **51**, 868–869 (1963).
77. B. Städler, T. M. Blättler, and A. Franco-Obregón, "Time-lapse imaging of in vitro myogenesis using atomic force microscopy," *J. Microsc.* **237**(1), 63–69 (2010).
78. E. Ralston, "Changes in architecture of the Golgi complex and other subcellular organelles during myogenesis." *J. Cell Biol.* **120**(2), 399–409 (1993).

Cristina Martinez-Torres obtained a BSc in biophysics from the Autonomous University of San Luis Potosi, Mexico. During her undergraduate studies, she was involved in several research groups, working in topics such as bioinformatics, cellular biology, biophysics, optical engineering, and atomic physics. Currently, she is a PhD student in the group of Françoise Argoul at the Ecole Normale Suprieure de Lyon, France, where she studies cell dynamics.

Lotfi Berguiga received his PhD in physics from the University of Burgundy in France in 2001, where he worked in near field optics. Since 2004, he has worked at the Ecole Normale Suprieure de

Lyon, where he has investigated surface plasmon microscopy. Since 2007, he has worked as research engineer at the French National Centre for Scientific Research, and his research interests include development of new techniques of microscopy applied to cell biology.

Laura Streppa obtained her MSc with honors in biomolecular research from University of Urbino "Carlo Bo" and performed three years compulsory and volunteer internship in different laboratories (microbiology, molecular biology, biochemistry, and physics). She is currently a first-year PhD student at PHAST of Lyon. Her thesis, titled "Biomechanical study of neuromuscular junction and its impact in myopathies," is supported by AFM Telethon and is a collaboration between Laboratory of Physics and LMBC of ENS.

Elise Boyer-Provera graduated in optics and industrial visual systems from the Engineering School of Telecom in Saint Etienne in 2010. After a three-year training in the private company Thales Angenieux, she was hired as an engineer at Ecole Normale Suprieure de Lyon to develop original microscopy devices based on surface plasmon microscopy and quantitative phase microscopy.

Laurent Schaeffer obtained his PhD thesis in molecular biology in 1995 from the University of Strasbourg, France. He is presently the head of the Center of Cell Biotechnology of Lyon Hospitals and the director of the Laboratory of Molecular Biology of the Cell in ENS Lyon. He currently studies the mechanisms that control muscle and neuromuscular junction formation and maintenance with a special focus on the control of muscle gene expression by neural cues.

Juan Elezgaray is a senior researcher at CNRS, in the unit CBMN (UMR 5248, Pessac, France). He received his PhD in theoretical physics from Paris 6 University in 1989. He has held a permanent position at CNRS since 1989. His scientific interests are focused on modeling biologically motivated systems, from proteins to DNA; he also develops optics-related modeling.

Alain Arneodo got his thesis in elementary particle physics from the University of Nice, France, in 1978. He is the director of research at CNRS and has published over 200 peer-reviewed papers. His scientific contribution encompasses many fields of modern physics, including statistical mechanics, dynamical systems theory, fully developed turbulence, the mathematics of fractals and multifractals, signal and image processing, wavelet transform analysis, and its applications in physics, geophysics, astrophysics, chemistry, biology, and finance.

Françoise Argoul received her PhD from the University of Bordeaux in 1986. She is director of research at CNRS and has coauthored over 110 peer-reviewed papers. She manages a research program in Laboratory of Physics of Ecole Normale Superieure of Lyon, devoted to the experimental characterization of the mechanical and genomic response of cellular systems under external stress and to the role of mechanical and dynamical parameters on the modification of cellular mechanims.